Low-temperature paramagnetic phase reentrance in praseodymium-doped manganites

Diego Carranza-Celis,[1] Christian T. Wolowiec,[2] Ali C. Basaran,[2] Pavel Salev,[3]
Ivan K. Schuller,[2] and Juan Gabriel Ramirez[1,2]

[1]*Department of Physics, Universidad de los Andes, Bogotá 111711, Colombia*
[2]*Department of Physics and Center for Advanced Nanoscience, University of California, San Diego, La Jolla, California 92093, USA*
[3]*Department of Physics and Astronomy, University of Denver, Denver, Colorado 80208, USA*

(Received 21 September 2023; accepted 16 April 2024; published 1 May 2024)

While the connection between colossal magnetoresistance and phase separation in praseodymium-doped rare-earth manganites has been well established, the underlying mechanisms enabling this connection still need to be fully understood. This paper thoroughly examines the phase separation in $La_{5/8-x}Pr_xCa_{3/8}MnO_3$ ($x = 0.40$) using an integrated approach including magnetotransport, electron spin resonance, and magnetic susceptibility. We observed that the initially fluidlike magnetic phase separation at intermediate temperatures transforms into the solidlike phase separation via a glass transition at low temperatures. Magnetization dynamics measurements revealed that this transition is concurrent with the reentrance of the paramagnetic phase. Our findings offer a perspective on the freezing of phase separation fluidlike behavior resulting in the advent of the low-temperature solidlike state, contributing to a deeper understanding of the temperature-dependent behaviors of praseodymium-doped rare-earth manganites.

DOI: 10.1103/PhysRevMaterials.8.054401

I. INTRODUCTION

Mixed valence manganites are strongly correlated systems in which the interplay between different electronic degrees of freedom gives rise to exotic transport and magnetic properties. For instance, the simultaneous double exchange interaction between Mn ions and electron-phonon coupling results in a remarkable sensitivity of electrical resistance to magnetic fields. This phenomenon has been a primary driving force for the extensive exploration of rare-earth manganites [1]. Manganites often exhibit a phase separation (PS) phenomenon—a spatial coexistence of different electronic and magnetic phases in a broad range of temperatures and magnetic fields, whose origin is not fully understood [2–5]. The closely intertwined interplay between distinct coexistent electronic phases gives rise to extraordinary functional properties. For example, spintronic [6], memristive [7], magnetocaloric [8], and photoelectric [9] effects have been linked to PS in manganites, making the control and understanding of these phenomena a burgeoning frontier in research.

In Pr-doped lanthanum manganites, the competing phases typically are ferromagnetic metal (FMM) and antiferromagnetic charge ordered insulator (AFM-COI) [10,11]. The AFM-COI phase emerges at $T_N \approx 140$ K from the parent paramagnetic COI phase in which Mn^{3+} and Mn^{4+} ions are ordered forming a lattice superstructure. Upon lowering temperature further, FMM phase clusters begin to grow within the AFM-COI matrix [12]. In a broad range of temperatures, both FMM and AFM-COI regions can be present in the material leading to the emergence of PS [13,14]. The cause of PS is often attributed to doping-induced chemical disorder [15]. In addition, the PS state can manifest two distinct behaviors: fluid phase separation (FPS) and static phase separation (SPS). The FPS typically occurs at intermediate temperatures [16], where the boundaries between the AFM-COI and FMM regions can move easily in response to changing temperatures or applying of external magnetic or electric fields [13,17,18]. The SPS appears when the FPS dynamics freeze at lower temperatures [4,10,16]. The transition from the FPS state to the SPS state is a glass transition where the phase boundary and spin dynamics slow down simultaneously [4,10]. Such glassy behavior at lower temperatures results from the competition between the FMM and AFM-COI phases, seemingly yielding multiple metastable states separated by presumably high-energy barriers in a complex free-energy landscape [10,17].

The mechanism behind the FPS-SPS transition is not fully understood. The prevalent hypothesis is that the phase competition is due to strain accommodation [4]. The strain accommodation may arise from the low-temperature reentering of the COI phase, which grows within a FMM matrix in a martensiticlike manner [19,20]. This implies that the crystal rapidly transforms into the COI phase through collective atomic movements [3]. Although a long-range propagation of the COI phase can be expected due to its martensiticlike nature, such propagation in fact should be rather local due to the disorder induced by the Pr doping [4,16]. At lower temperatures, local martensiticlike transformations (and the resulting strain accommodation) could create an SPS state between the AFM-COI and FMM phases. The SPS has local strain order but is disordered on the global sample scale. Therefore, the SPS state in manganites is usually associated with a strained-glass state [4,21,22]. Despite the prevalence of the COI reentrance hypothesis in explaining the FPS-SPS transition, there is a lack of experimental evidence to support it. Additionally, the factors underlying the reappearance of a COI phase at low temperatures remain mainly unknown.

This paper investigates the phase separation features and the FPS-SPS transition in $La_{5/8-x}Pr_xCa_{3/8}MnO_3$ (LPCMO)

with $x = 0.40$ as the prototypical Pr-doped rare-earth manganite system displaying natural phase separation. We augmented the magnetotransport and AC susceptibility measurements with the temperature-dependent magnetic resonance studies. The sensitivity and phase selectivity of magnetic resonance allowed us to identify subtle phase transition features that remain hidden in conventional magnetometry experiments. The resonance measurements revealed the recovery of the electronic paramagnetic resonance (EPR) mode coinciding with the FPS-SPS transition, providing direct experimental evidence of the paramagnetic phase reentrance at low temperatures. The resonance observations were further supported by the AC susceptibility measurements showing a glass transition and magnetometry showing a decrease of spontaneous magnetization associated with the paramagnetic phase reentrance. Additionally, the resonance measurements detected a weak ferromagnetic resonance (FMR) mode at high temperatures, possibly due to a Griffiths-like phase, and the development of two distinct FMR modes at intermediate temperatures that displayed dissipative features related to the fluidlike behavior. This paper demonstrates that probing magnetization dynamics in resonance experiments provides unique insights into the complex nature of phase transitions in strongly correlated systems, where subtle magnetic signatures of one phase can be overshadowed by the strong response of other phases in the phase coexistence state.

II. METHODS

$La_{5/8-x}Pr_xCa_{3/8}MnO_3$ ($x = 0.40$) was fabricated using a solid-state reaction. High-purity oxides La_2O_3 (99.999%), Pr_6O_{11} (99.996%), and MnO_2 (99.996%) and the high-purity carbonate $CaCO_3$ (99.999%) were carefully weighted—using appropriate stoichiometric amounts—and mixed in agate mortar until obtaining a homogeneous powder. Before weighing, the rare-earth oxides were preheated at 1000 °C for 12 h. The MnO_2 and $CaCO_3$ reagents were maintained at 100 °C for several days [23,24]. The mixed powders were heated at 1050 °C for 12 h, grounded for 4 h in an agate mortar (adding an appropriate amount of isobutyl alcohol), reheated at 1050 °C for 12 h, and grounded again for 4 h. Afterwards, the powder was dried and pelletized under a pressure of 2.0×10^6 Pa and heated at 1350 °C for 12 h in a tubular furnace. The resulting pellets were reground, repelletized, and heated at 1350 °C for 48 h [23,24]. The LPCMO phase formation was confirmed by x-ray diffraction (see Fig. S1 in Supplemental Material [25]). Rietveld refinement of the x-ray data was performed using the GSAS-II software [26].

We used a combination of resistance as a function of temperature (R-T) and magnetoresistance (R-H) measurements to obtain the temperature–magnetic-field phase diagram. We collected $0 \rightarrow 40 \rightarrow 0$-kOe cycle MR data (5-kOe/min sweep rate) within a 10–150-K temperature range (at 10-K steps) using a conventional four-wire configuration. Before measuring each R-H curve, the sample was heated to 250 K and cooled to the measurement temperature to reset the phase separation state. Resonance measurements were performed with 1-K steps while cooling the sample from 230 to 35 K. The DC field was swept between 0 and 9 kOe at 10 Oe/s. The microwave power was 1 mW. AC susceptibility was probed using AC excitation magnetic fields of 137, 2508, and 5131 Hz with 4-Oe amplitude.

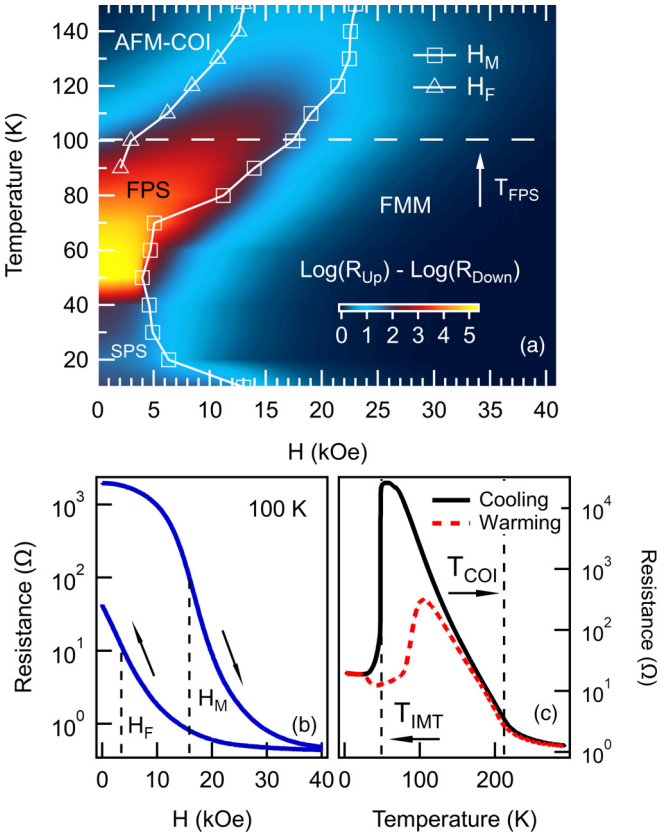

FIG. 1. (a) Phase diagram of $La_{5/8-x}Pr_xCa_{3/8}MnO_3$ ($x = 0.40$). Symbols represent the maximum derivatives of the R-H curves for the increasing and decreasing field branches corresponding to melting and freezing fields, H_M and H_F, respectively. The color map is the difference between the logarithm of R-H branches for increasing and decreasing magnetic field. (b) An example of an R-H curve at 100 K used to plot the phase diagram in panel (a). The arrows indicate increasing and decreasing field R-H branches. H_M and H_F correspond to the maximum R-H slope. (c) Resistance as a function of temperature. COI and IMT transitions are highlighted.

III. RESULTS AND DISCUSSIONS

We obtained the temperature–magnetic-field phase diagram of the LPCMO sample using magnetotransport measurements [Fig. 1(a)]. Mapping the phase states allowed us to identify two transition types: (i) AFM-COI to FMM phase and (ii) FPS to SPS state. As discussed further, the phase diagram is also crucial for interpreting the magnetic resonance and AC susceptibility measurements. The phase mapping procedure followed Ref. [16]. At each temperature, we recorded an R-H curve for a $0 \rightarrow 40 \rightarrow 0$-kOe cycle [an example curve acquired at 100 K is shown in Fig. 1(b)]. For each curve, we took the difference between the log(R)-H curves for the field ramping up and ramping down branches [indicated with arrows in Fig. 1(b)]. The color map in the phase diagram [Fig. 1(a)] corresponds to this resistance logarithm difference between ramp-up and ramp-down branches: bright color indicates a highly hysteretic R-H dependence (i.e., facile AFM-COI-to-FMM

phase conversion by the applied field), while dark color corresponds to nearly identical *R-H* ramping up/down curves (stable AFM-COI and FMM phases upon field sweeping). The square and triangle symbols in the phase diagram indicate melting (H_M) and freezing (H_F) fields, respectively. The H_M and H_F transition fields were obtained from the maximum *R-H* slope of the field ramping (up/down) branches.

The phase diagram of the LPCMO sample [Fig. 1(a)] shows several important features.

(i) The AFM-COI phase is dominant at high temperatures and low magnetic fields.

(ii) The FMM phase emerges at low temperatures and high fields.

(iii) The AFM-COI and FMM phase coexistence is present at intermediate temperatures.

This region, which exhibits the largest log(R)-H difference, is delimited by melting and freezing fields (H_M and H_F) and is labeled as FPS. In the FPS region, coexisting AFM-COI and FMM phases are readily converted into each other by changing the magnetic field. This behavior indicates that the phase boundaries are unpinned, resulting in a fluidlike behavior [4,16]. H_F increases rapidly below 30 K. Such an increase is associated with the FPS-SPS transition, i.e., where the fluidlike behavior of the separated phases freezes producing a static phase coexistence. We further identified the COI transition at $T_{\mathrm{COI}} = 212$ K by observing a sudden slope change in the *R-T* curve [Fig. 1(c)]. The *R-T* curve also exhibits an insulator-to-metal transition (IMT) at $T_{\mathrm{IMT}} = 50$ K, where resistance changes by about three orders of magnitude [Fig. 1(c)]. The IMT occurs inside the FPS region in the phase diagram. Overall, the phase diagram in Fig. 1(a) determines the temperature and magnetic-field transitions between the AFM-COI and FMM phases. Additionally, it identifies the regions where these two phases coexist and defines the boundaries of the FPS and SPS states. This allows us to correlate the LPCMO phase state to the changes observed in the magnetic resonance and AC susceptibility measurements.

We performed AC susceptibility measurements at different frequencies of the AC driving field to investigate whether a glass transition occurs during the transition to the SPS state and to identify other possible magnetic transitions. Figure 2(a) shows the real component of AC susceptibility, χ', measured at a frequency of 137 Hz. A peak can be identified at the charge ordering transition at $T_{\mathrm{COI}} = 212$ K. The peak associated with COI is also clearly visible in the χ' derivative [see Fig. S2(a) in Supplemental Material [25]]. The χ' derivative plot further shows Neel temperature at $T_N = 140$ K and Curie temperature at $T_C = 50$ K. Curie temperature coincides with the IMT [highlighted in the *R-T* curve in Fig. 1(c)]. Cooling and warming branches of the χ' curve bifurcate to about 30 K. The closing of the χ' hysteresis around 30 K coincides with the appearance of a broad peak in the AC susceptibility imaginary component, χ" [Fig. 2(b)]. Interestingly, this peak shifts to higher temperatures with increasing AC field frequency [Fig. 2(c), black symbols]. A second peak can be observed in χ" near 100 K [Fig. 2(b)]. This peak also shifts to higher temperatures with increasing the AC field frequency [Fig. 2(c), red symbols]. Comparing these χ" features to the phase diagram in Fig. 1(a) reveals that the low-temperature χ" peak coincides with the SPS transition, while the high-temperature

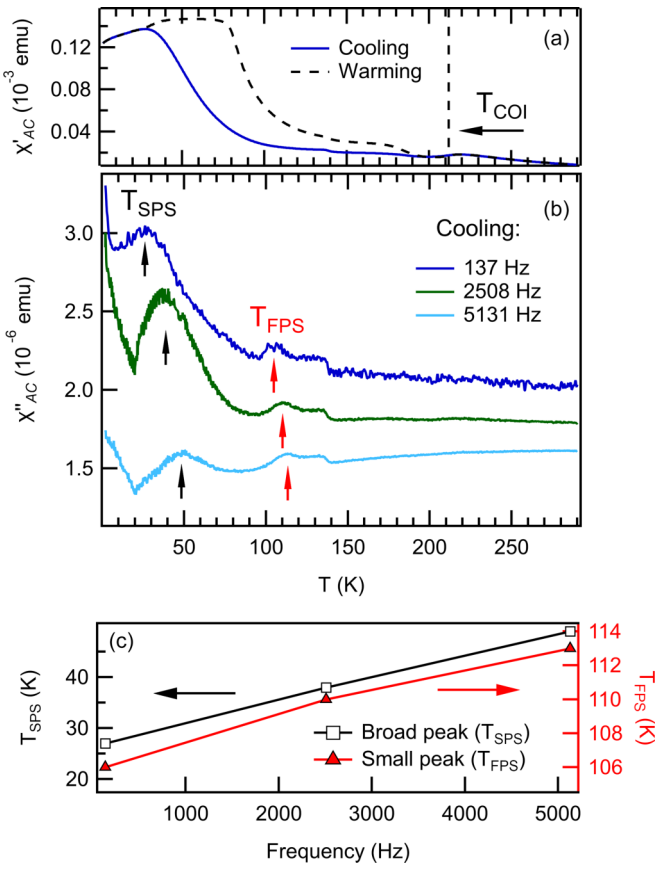

FIG. 2. (a) Real component of the AC susceptibility as a function of temperature. (b) The imaginary part of the AC susceptibility as a function of temperature at three different frequencies. Arrows indicate two peaks, near 50 and 100 K, that shift with frequency and are associated with the SPS and FPS transitions, respectively. (c) Frequency dependence of the temperature of the imaginary susceptibility peaks at low (black symbols) and high (red symbols) temperatures extracted from the data in panel (b).

χ" peak occurs at the FPS transition. The frequency dependence of these peaks suggests that the SPS and FPS transition involve dissipative processes. They correspond to the irreversible movement of boundaries of separated phases in the FPS state and the glassy behavior in the SPS state that causes the freezing of the fluidlike behavior. Such glassy behavior can be caused by strain accommodation at low temperatures and produce a slowing down of magnetization dynamics [4], evidenced by the peak of χ" near 30 K.

Temperature-dependent magnetic resonance measurements further revealed complex evolution of the magnetism dynamics in LPCMO. Figure 3(a) shows the color map formed by isothermal resonance curves in the 35–230-K temperature range at 1-K steps and in the 1–9-kOe field. The resonance fields, H_R, obtained from Lorentzian fits (solid symbols) of the isothermal resonance curves, are shown in Fig. 3(a). Figures 3(b) and 3(c) further show the integrated intensity and linewidth of the fitted resonance curves. The integrated intensity corresponds to the double numerical integration of the fitted curves. As the experimental resonance signal gives the derivative of microwave absorption, the first integration restores the absorption curve and the second integration yields

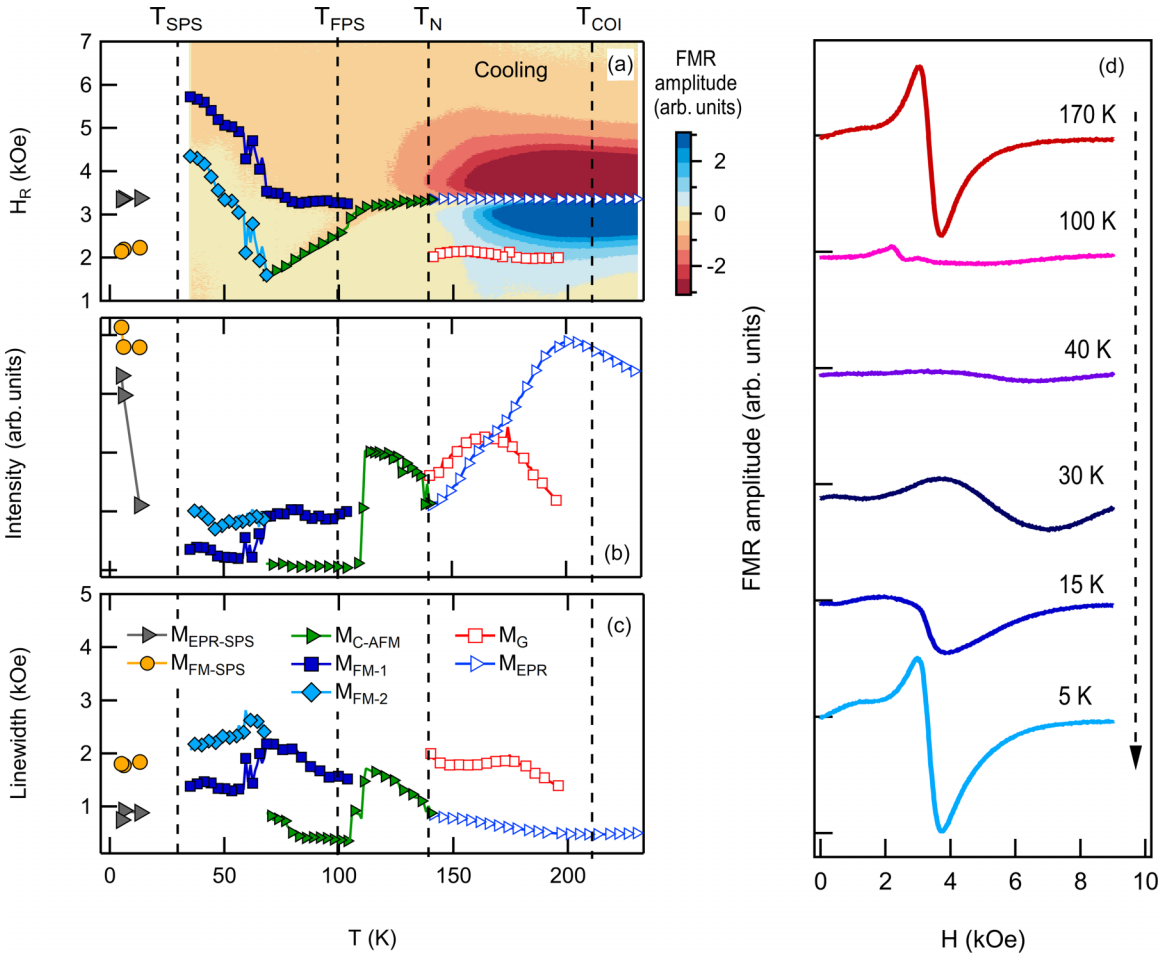

FIG. 3. (a) Magnetic resonance density as a function of temperature. Symbols are the resonance fields obtained from Lorentzian fitting. (b, c) Integrated intensity and linewidths obtained from the Lorentzian fit of the resonance data in panel (a). Blue triangles (M_{EPR}) and red squares (M_G) describe the resonance of the high-temperature paramagnetic and Griffiths-like phases, respectively. Green triangles ($M_{C-\mathrm{AFM}}$) correspond to the resonance of the canted AFM phase. Dark blue squares ($M_{\mathrm{FM}-1}$) and light blue rhombs ($M_{\mathrm{FM}-2}$) show the resonance features of the modes due to the FMM phase in the FPS state. Finally, at low temperatures, gray triangles ($M_{\mathrm{EPR}-\mathrm{SPS}}$) and yellow circles ($M_{\mathrm{FM}-\mathrm{SPS}}$) describe the resonance of the paramagnetic and ferromagnetic phases in the SPS state, respectively. (d) Examples of magnetic resonance signals at a few select temperatures. The close resemblance of the 170- and 5-K curves is indicative of the paramagnetic phase reentrance at low temperatures.

the absorption curve area, which is commonly used as a measure of the resonance intensity. Several resonance curve examples and their fitting are presented in Fig. S4 in the Supplemental Material [25]. We observed two types of resonances in the measured signals: EPR and FMR. EPR modes are associated with the paramagnetic phase. In EPR, the unpaired spins of $Mn^{4+} - Mn^{3+}$ ions precess around an external DC magnetic field, reaching resonance when exposed to an electromagnetic wave of the appropriate frequency. On the other hand, FMR modes are associated with the ferromagnetic phase. FMR operates on the same principle as EPR, but resonance is achieved by the magnetic moment formed by ferromagnetically coupled spins. FMR frequency depends strongly on the saturation magnetization and on the demagnetizing and anisotropy fields of the sample [27].

At high temperatures (above 140 K), the measured signal originates mainly from the EPR mode M_{EPR} [blue triangles in Fig. 3(a)] likely due to the $Mn^{4+} - Mn^{3+}$ ions. A second resonance mode M_G (red squares) emerges in the 140–198-K range where LPCMO is supposed to be paramagnetic. The second resonance is almost hidden below the strong EPR signal but can be identified in the fitting. We attribute this weak resonance mode to the random ferromagnetic clusters inside the paramagnetic LPCMO [28]. The ferromagnetic clusters are often observed above the Curie temperature (T_C) in mixed-valence manganites and have been widely associated with a Griffiths-like phase [28–30]. The integrated intensity of the M_{EPR} mode increases until it reaches the maximum around 200 K, where the M_G mode emerges [Fig. 3(b)]. The M_{EPR} mode linewidth increases while cooling just below T_{COI}, suggesting that the broadening is likely caused by the charge ordering [Fig. 3(c)]. The charge ordering also has a similar effect on the M_G mode as its linewidth also becomes broader. It has been argued that the COI phase is necessary to obtain ferromagnetic clusters randomly located in mixed-valence manganites [28]. Therefore, the appearance of this second M_G mode below T_{COI} agrees with the expectations for the temperature evolution of LPCMO magnetic properties.

The resonance field of the primary mode shows a slight decrease below the AFM transition at $T_N = 140$ K [green triangles in Fig. 3(a)], while the M_G mode disappears completely. A zoomed-in view, displaying the sudden decrease in the resonance field near T_N, can be observed in Fig. S2 in Supplemental Material [25]. Because AFM resonance could be detected only in high magnetic fields and high frequencies [31,32], the resonance signal below T_N, labeled as $M_{C-\mathrm{AFM}}$, could be due to the net magnetization of the canted antiferromagnetic phase that emerges in the regions lacking charge ordering [33–37]. In contrast, the AFM regions with charge ordering (AFM-COI phase) do not have canted spins and should not contribute to the resonance signal. As temperature approaches T_N, the integrated intensity of the M_{EPR} mode decreases rapidly, indicating the volume fraction reduction of the paramagnetic phase [Fig. 3(b)]. In contrast, the integrated intensity of the $M_{C-\mathrm{AFM}}$ mode increases below T_N. The resonance linewidth exhibits a discontinuity at the AFM transition and keeps increasing as the temperature decreases [Fig. 3(c)]. Therefore, the resonance field, integrated intensity, and linewidth analysis provide strong evidence that a different resonance mode emerges at T_N.

When LPCMO enters the FPS region below 100 K (according to the phase diagram in Fig. 1 and AC susceptibility measurements in Fig. 2), a new mode emerges signifying the phase coexistence [Fig. 3(a)]. We label this mode $M_{\mathrm{FM}-1}$ (dark blue squares), which is an FMR mode that presumably corresponds to the FMM phase, as the mode appears with the emergence of FMM regions. The integrated intensity of the $M_{\mathrm{FM}-1}$ mode is much larger than that of the $M_{C-\mathrm{AFM}}$ mode [Fig. 3(b)] and $M_{C-\mathrm{AFM}}$ abruptly decays at 100 K. This suggests that a considerable fraction of the canted AFM phase transforms into the FMM phase. It has been widely accepted that chemical disorder induced by Pr doping in LPCMO can promote the formation of regions lacking charge ordering at temperatures below T_{COI}, and a canted AFM phase can emerge in these regions at T_N [33–37]. Such regions are the most probable sites of the FMM phase formation and growth [37]. Therefore, our observation of the sudden rise of the $M_{\mathrm{FM}-1}$ mode and the coinciding decay of the $M_{C-\mathrm{AFM}}$ mode is consistent with the hypothesis that the FMM phase emerges in the regions with canted AFM moments [37]. In the FPS region, below 100 K, the linewidths of $M_{C-\mathrm{AFM}}$ and $M_{\mathrm{FM}-1}$ modes increase as temperature decreases [Fig. 3(c)]. As was discussed earlier, the AC susceptibility measurements indicated the onset of phase boundary movement in the FPS region [frequency dependent peaks in Figs. 2(b) and 2(c)]. Therefore, the resonance mode broadening can be correlated with the fluidlike behavior because the rapid phase boundary movement could contribute to the magnetization dynamics damping [38].

A sudden resonance field increase can be observed at 70 K [Fig. 3(a)], suggesting an accelerated growth of the FMM phase. The resonance measurements revealed two FMR modes that we label $M_{\mathrm{FM}-1}$ (dark blue squares) and $M_{\mathrm{FM}-2}$ (light blue rhombs). Both modes show the H_R increase with decreasing temperature, which can be attributed to the increased saturation magnetization and FMM volume fraction expansion. The FMM phase growth could be promoted by the large magnetic field, up to 9 kOe, used to acquire the resonance data. This high magnetic field can melt a significant fraction of AFM regions within the AFM-COI matrix, as suggested by the phase diagram in Fig. 1(a). Consequently, the canted antiferromagnetic $M_{C-\mathrm{AFM}}$ mode disappears, and the ferromagnetic $M_{\mathrm{FM}-2}$ mode emerges. The integrated intensity of $M_{\mathrm{FM}-2}$ increases suddenly when the $M_{C-\mathrm{AFM}}$ vanishes [Fig. 3(b)], consistent with the AFM phase melting. The linewidths of the $M_{\mathrm{FM}-1}$ and $M_{\mathrm{FM}-2}$ modes decrease with decreasing temperature [Fig. 3(c)]. This observed narrowing of the FMR resonance peaks suggests that a large fraction of LPCMO enters the FMM state, which lowers the phase boundary density, reducing their contribution to the magnetization precession dampening. The development of two FMR modes can be due to the presence of FMM regions with different sizes and morphologies. One of the FMR modes may originate from small isolated ferromagnetic clusters, while the other mode corresponds to larger coalesced regions. Previous micromagnetic calculations have suggested this possibility [39]. Stabilization of an intermediate state in LPCMO consisting of nanoscale FMM and COI domains that coexist with larger, microscale FMM and COI domains has been also suggested in photoexcitation experiments [40]. Although our experiments did not involve photoexcitation and our LPCMO samples had slightly different composition than in Ref. [40], it is possible that the sensitivity of resonance measurements enabled detecting the responses of both microscale FMM domains and nanoscale FMM domains in the intermediate state, which produced the two distinct FMR modes. The polycrystalline nature of our LPCMO sample can also contribute to the development of two FMR modes. Polycrystallinity implies independent grain resonance. Variations in grain orientation can result in two contributions to the resonance signal. One corresponds to the grains with the easy axis of crystalline anisotropy aligned along the DC field, used to acquire the resonance data. The other corresponds to the grains with the hard axis aligned along this DC field [41–43].

Finally, we observed the recovery of an EPR mode at temperatures below 35 K. This low-temperature region corresponds to the entering of the SPS state according to the phase diagram in Fig. 1. In the SPS state, there are two resonance modes that we label $M_{\mathrm{FMR}-\mathrm{SPS}}$ (orange circles) and $M_{\mathrm{EPR}-\mathrm{SPS}}$ (gray triangles) in Fig. 3(a). Both low-temperature resonance modes show an abrupt H_R decrease compared to the two FMR modes at higher temperatures. The $M_{\mathrm{FMR}-\mathrm{SPS}}$ mode at the resonance field of $\approx$2.23 kOe has high integrated intensity that depends weakly on temperature [Fig. 3(b)], and a broad linewidth of $\approx$1.78 kOe [Fig. 3(c)], and can be identified as the FMR mode. Interestingly, the integrated intensity of the second mode $M_{\mathrm{EPR}-\mathrm{SPS}}$ at the resonance field of $\approx$3.34 kOe increases rapidly with decreasing temperature [Fig. 3(b)], while its linewidth is much narrower, only 0.92 kOe [Fig. 3(c)]. Because the resonance field, integrated intensity, and linewidth of the low-temperature $M_{\mathrm{EPR}-\mathrm{SPS}}$ mode as well as its shape [compare 5- and 170-K curves in Fig. 3(d)] are nearly identical to those of the high-temperature M_{EPR} mode, we conclude that the $M_{\mathrm{EPR}-\mathrm{SPS}}$ mode is due to the reentrance of the paramagnetic phase when LPCMO transitions into the SPS state. The observed resonance field of the $M_{\mathrm{EPR}-\mathrm{SPS}}$ mode is also virtually equal (3.35 kOe) to that obtained from the Larmor frequency equation for free

electrons [27], for the 9.4-GHz microwave frequency used in our experiments. This supports further that the low-temperature $M_{\mathrm{EPR-SPS}}$ mode is an EPR mode. The reentrance of the paramagnetic phase observed in the resonance experiments is also consistent with the saturation magnetization decrease at low temperatures found in magnetometry measurements [see Fig. S2(b) in Supplemental Material [25]] and observed peaks in the AC susceptibility that indicate a phase transition in LPCMO as it enters the SPS state (Fig. 2). Resonance measurements while warming showed similar results of the emergence of two $M_{\mathrm{EPR-SPS}}$ and $M_{\mathrm{FMR-SPS}}$ modes in the SPS state (see Fig. S3 in Supplemental Material [25]), indicating consistency of our observations. The low-temperature paramagnetic phase can be expected to have charge ordering and grow in a martensiticlike way resulting in strain accommodation [4,19,20]. The formation of a new phase separation state between the FMM and reentrant paramagnetic phase in which the strain accommodation hinders the phase boundary movement can be responsible (i) for the freezing of easy field-driven phase conversion in the SPS state observed in the magnetotransport measurements (Fig. 1) as well as (ii) for the glassy dynamics found in the magnetic susceptibility measurements at low temperatures (Fig. 2).

Our results suggest that below the SPS state the AFM-COI and FMM phases coexist with a paramagnetic phase. The reentrance of the paramagnetic phase cannot be unambiguously identified using DC magnetometry because the strong signal of the FMM phase overshadows weak paramagnetic contributions. Conventional measurements reveal changes in saturation magnetization, susceptibility, and magnetotransport properties across the FPS-SPS transition, but do not provide information about the physical origin behind these changes. The ability of resonance experiments to resolve individual FMR and EPR modes is indispensable to identify the phase state evolution in LPCMO, which highlights the great utility of spin resonance spectroscopy methods to unravel intricate coexisting magnetic phases in phase-separated systems.

IV. CONCLUSIONS

Using combined magnetotransport and magnetism dynamics measurements, we studied the phase separation in an archetypical manganite system $La_{5/8-x}Pr_xCa_{3/8}MnO_3$ ($x = 0.40$). Our magnetic resonance experiments uncovered multiple unique features in all phase states of LPCMO over a broad temperature range. At high temperatures, we observed the coexistence of strong EPR and weak FMR modes, which indicates the presence of small ferromagnetic clusters inside the paramagnetic matrix, likely a Griffiths-like phase. In the FPS state at intermediate temperatures, we found the emergence of two distinct FMR modes that display significant linewidth broadening. This linewidth broadening can be attributed to the irreversible phase boundary movement, which is responsible for the AFM-COI to FMM phase conversion by the external magnetic field. In the low-temperature SPS regime, our resonance measurements directly revealed the reentrance of a paramagnetic phase coinciding with the freezing of the FPS dynamics. The strain accommodation associated with the paramagnetic phase reentrance can be responsible for the glassy behavior of the FPS-SPS transition, shown by the AC susceptibility. Our paper offers a perspective on studying the phase separation phenomenon in Pr-doped manganites. Our observations suggest that it is necessary to include the emergence of a paramagnetic phase in models that aim at explaining the low-temperature metastable glassy state. The experimental findings in this paper were enabled by the sensitivity and phase selectivity (i.e., the ability to separate different FMR and EPR modes) of magnetic resonance, making it an ideal technique to explore hidden phases in a broad range of materials with multiple coexisting magnetic phases, where a strong signal from one magnetic phase might mask the response of other phases in conventional magnetometry.

ACKNOWLEDGMENTS

J.G.R. and D.C.-C. acknowledge support from Facultad de Ciencias and Vicerrectoría de investigaciones Universidad de los Andes, Convocatoria Facultad de Ciencias, Project No. INV-2022-150-2627. J.G.R. acknowledges support from the Facultad de Ciencias and Vicerrectoría de investigaciones of Universidad de los Andes during Semestre de trabajo académico independiente (STAI) at University of California, San Diego. This work was also supported by Project No. INV-2021-128-2313 of the Faculty of Science at Universidad de los Andes, Bogotá, Colombia. The research at University of California, San Diego was supported by the U.S. Department of Energy's Office of Basic Energy Science, under Grant No. DE-FG02-87ER45332.

[1] E. Dagotto, *Nanoscale Phase Separation and Colossal Magnetoresistance: The Physics of Manganites and Related Compounds*, Springer Series in Solid-State Sciences (Springer, Berlin, 2003).

[2] Y. Zhu, K. Du, J. Niu, L. Lin, W. Wei, H. Liu, H. Lin, K. Zhang, T. Yang, Y. Kou, J. Shao, X. Gao, X. Xu, X. Wu, S. Dong, L. Yin, and J. Shen, Nat. Commun. **7**, 11260 (2016).

[3] H. Zhou, L. Wang, Y. Hou, Z. Huang, Q. Lu, and W. Wu, Nat. Commun. **6**, 8980 (2015).

[4] P. A. Sharma, S. B. Kim, T. Y. Koo, S. Guha, and S. W. Cheong, Phys. Rev. B **71**, 224416 (2005).

[5] T. Miao, L. Deng, W. Yang, J. Ni, C. Zheng, J. Etheridge, S. Wang, H. Liu, H. Lin, and Y. Yu, Proc. Natl. Acad. Sci. USA **117**, 7090 (2020).

[6] W. Yang, Q. Shi, T. Miao, Q. Li, P. Cai, H. Liu, H. Lin, Y. Bai, Y. Zhu, Y. Yu, L. Deng, W. Wang, L. Yin, D. Sun, X.-G. Zhang, and J. Shen, Nat. Commun. **10**, 3877 (2019).

[7] W. R. Acevedo, D. Rubi, J. Lecourt, U. Lüders, F. Gomez-Marlasca, P. Granell, F. Golmar, and P. Levy, Phys. Lett. A **380**, 2870 (2016).

[8] P. Amirzadeh, H. Ahmadvand, P. Kameli, B. Aslibeiki, H. Salamati, A. G. Gamzatov, A. M. Aliev, and I. K. Kamilov, J. Appl. Phys. **113**, 123904 (2013).

[9] X. Chai, H. Xing, and K. Jin, Sci. Rep. **6**, 23280 (2016).

[10] W. Wu, C. Israel, N. Hur, S. Park, S.-W. Cheong, and A. de Lozanne, Nat. Mater. **5**, 881 (2006).

[11] M. Uehara, S. Mori, C. H. Chen, and S.-W. Cheong, Nature (London) **399**, 560 (1999).

[12] J. L. García-Muñoz, A. Collado, M. A. G. Aranda, and C. Ritter, Phys. Rev. B **84**, 024425 (2011).

[13] L. Zhang, C. Israel, A. Biswas, R. L. Greene, and A. de Lozanne, Science **298**, 805 (2002).

[14] E. Dagotto, T. Hotta, and A. Moreo, Phys. Rep. **344**, 1 (2001).

[15] K. F. Wang, Y. Wang, L. F. Wang, S. Dong, D. Li, Z. D. Zhang, H. Yu, Q. C. Li, and J.-M. Liu, Phys. Rev. B **73**, 134411 (2006).

[16] T. Dhakal, J. Tosado, and A. Biswas, Phys. Rev. B **75**, 092404 (2007).

[17] L. Ghivelder and F. Parisi, Phys. Rev. B **71**, 184425 (2005).

[18] A. Shakya and A. Biswas, J. Appl. Phys. **127**, 213902 (2020).

[19] V. Podzorov, B. G. Kim, V. Kiryukhin, M. E. Gershenson, and S.-W. Cheong, Phys. Rev. B **64**, 140406(R) (2001).

[20] V. G. Sathe, A. Ahlawat, R. Rawat, and P. Chaddah, J. Phys.: Condens. Matter. **22**, 176002 (2010).

[21] V. Agarwal, G. Sharma, P. K. Siwach, K. K. Maurya, V. P. S. Awana, and H. K. Singh, Solid State Commun. **202**, 43 (2015).

[22] X. Ren, Phys. Status Solidi B **251**, 1982 (2014).

[23] J. A. Collado, C. Frontera, J. L. Garcia-Muñoz, C. Ritter, M. Brunelli, and M. A. G. Aranda, Chem. Mater. **15**, 167 (2003).

[24] H.-F. Li and T. Brückel, *Synthesis of CMR Manganites and Ordering Phenomena in Complex Transition Metal Oxides* (Forschungszentrum, Jülich, 2008).

[25] See Supplemental Material at http://link.aps.org/supplemental/10.1103/PhysRevMaterials.8.054401 for XRD powder diffractogram, additional magnetometry measurements, zoom in on the resonance field near the Neel temperature, resonance field obtained from Lorentzian fits while warming, and examples of resonance curves and their fittings.

[26] B. H. Toby and R. B. Von Dreele, J. Appl. Crystallogr. **46**, 544 (2013).

[27] J. M. D. Coey, *Magnetism and Magnetic Materials* (Cambridge University, Cambridge, England, 2010).

[28] V. N. Krivoruchko, Low Temp. Phys. **40**, 586 (2014).

[29] J. Deisenhofer *et al.*, Phys. Rev. Lett. **95**, 257202 (2005).

[30] C. Autret-Lambert, M. Gervais, S. Roger, F. Gervais, M. Lethiecq, N. Raimboux, and P. Simon, Solid State Sci. **71**, 139 (2017).

[31] S. Mitsudo, K. Hirano, H. Nojiri, M. Motokawa, K. Hirota, A. Nishizawa, N. Kaneko, and Y. Endoh, J. Magn. Magn. Mater. **177–181**, 877 (1998).

[32] A. I. Shames, A. Yu. Yakubovsky, and S. V. Gudenko, Magnetic phase separation in $La_{1-x}Ca_xMnO_3$ near half-doped composition observed by EMR, in *EPR in the 21st Century*, edited by A. Kawamori, J. Yamauchi, and H. Ohta, (Elsevier, Amsterdam, 2002), pp. 127–132.

[33] S. Angappane, M. Pattabiraman, G. Rangarajan, K. Sethupathi, and V. S. Sastry, Phys. Rev. B **69**, 094437 (2004).

[34] H. J. Lee, K. H. Kim, M. W. Kim, T. W. Noh, B. G. Kim, T. Y. Koo, S.-W. Cheong, Y. J. Wang, and X. Wei, Phys. Rev. B **65**, 115118 (2002).

[35] N. S. Bingham, P. Lampen, M. H. Phan, T. D. Hoang, H. D. Chinh, C. L. Zhang, S. W. Cheong, and H. Srikanth, Phys. Rev. B **86**, 064420 (2012).

[36] J. Q. He, V. V. Volkov, T. Asaka, S. Chaudhuri, R. C. Budhani, and Y. Zhu, Phys. Rev. B **82**, 224404 (2010).

[37] G. Singh-Bhalla, A. Biswas, and A. F. Hebard, Phys. Rev. B **80**, 144410 (2009).

[38] P. A. Sharma, S. El-Khatib, I. Mihut, J. B. Betts, A. Migliori, S. B. Kim, S. Guha, and S.-W. Cheong, Phys. Rev. B **78**, 134205 (2008).

[39] D. Carranza-Celis, E. Skoropata, A. Biswas, M. R. Fitzsimmons, I. K. Schuller, and J. G. Ramirez, Phys. Rev. Mater. **5**, 124413 (2021).

[40] H. Lin, H. Liu, L. Lin, S. Dong, H. Chen, Y. Bai, T. Miao, Y. Yu, W. Yu, J. Tang, Y. Zhu, Y. Kou, J. Niu, Z. Cheng, J. Xiao, W. Wang, E. Dagotto, L. Yin, and J. Shen, Phys. Rev. Lett. **120**, 267202 (2018).

[41] E. Schlömann, J. Phys. Chem. Solids **6**, 257 (1958).

[42] E. Schlömann, J. Phys. Radium **20**, 327 (1959).

[43] V. A. Zhuravlev, Phys. Solid State **41**, 956 (1999).